Equivalent transport models in atomistic quantum wires

Gennady Mil'nikov,* Nobuya Mori, and Yoshinari Kamakura
Graduate School of Engineering, Osaka University, 2-1 Yamada-oka, Suita, Osaka 565-0871, Japan and
CREST, JST, 5 Sanbancho, Chiyoda-ku, Tokyo 102-0075, Japan
(Received 10 November 2011; published 23 January 2012)

The paper presents low-dimensional quantum models for atomistic transport in nanowire field-effect transistors. A variational method is developed to construct a small representative basis which reproduces physical states of a tight-binding Hamiltonian within an arbitrary energy window. The equivalent transport models with the basis-transformed Hamiltonian are constructed and tested for various silicon nanowire transistors. The small size of the model makes it a powerful tool to study atomistic quantum transport in the presence of inelastic scattering.

DOI: 10.1103/PhysRevB.85.035317 PACS number(s): 73.23.−b, 73.40.Qv

I. INTRODUCTION

Recent progress in semiconductor device technologies has led to the development of a variety of novel devices such as double-gate transistors,[1] carbon nanotubes,[2] and gate-all-around (GAA) metal-oxide-semiconductor field-effect transistors (MOSFETs).[3–6] Continual technological innovations make it possible to create semiconductor structures with the MOS channel lengths on the order of 10 nm or even smaller.[7,8] Experimental studies of Ge/Si nanowire (NW) heterostructures have shown excellent gate control, high drain current, and reduced sensitivity to temperature.[9,10] The modern growth mechanisms[11] also enable one to modulate the composition of NWs along the growth axes and synthesize NW heterostructures with embedded tunnel barriers.[12,13] The NWs thus offer plenty of opportunities in quasi-one-dimensional physics and can also be considered to be promising candidates for nanoelectronics.[14] Detailed theoretical studies of the electronic transport in such devices can support the experimental research and help in addressing practical issues related to the development of MOSFETs with ultrashort channels.[15]

In the nanoscale regime, semiconductor NWs can no longer be treated as continuous systems within the effective mass approximation. The current characteristics or electric conductance are directly related to the electronic subband structure which depends on the size and growth direction of NW. Another important factor is the inelastic interaction of mobile carriers with lattice vibrations,[16] which is expected to strongly deteriorate the ON current of NWs in the nanoscale regime.[17,18] The nearest-neighbor tight-binding models with various levels of approximations are commonly used to account for realistic band structure in transport simulations.[19] In combination with the nonequilibrium Green's function (NEGF) method,[20,21] is has become a standard approach to quantum transport in semiconductor nanostructures.

In the ballistic regime, the inelastic processes can be neglected and NEGF becomes equivalent to the Landauer approach; that is, the nonequilibrium state of the device is described in terms of appropriate one-particle scattering wave functions. This is a great simplification compared to the full NEGF description. The recursive Green's function method[22,23] is commonly used to manage computation burden effectively in the ballistic regime. Recently developed atomistic R-matrix propagation technique[24–26] offers further improvements. Even in the ballistic regime, however, atomistic transport simulations in realistic nanostructures with thousands of atoms require substantial computational resources.

Modeling inelastic scattering processes is computationally much more challenging. The NEGF formalism provides a regular approach to account for the inelastic effects but it requires self-consistent calculations of the total Green's functions in order to characterize the spectrum of quasiparticle states and their occupation. In the scope of the tight-binding models, the size of Green's function matrices is the total number of atomic orbitals which can reach millions of states in realistic nanostructures. Dealing with such huge complex-valued matrices is prohibitively difficult in terms of both storage capacity and computational time. Most of the simulators with the dissipative scattering are based on the effective mass model and mode space approach.[27–29] Full band simulations of a Si NW transistor have been also reported recently, but limited computer resources necessitates extra simplifications in the NEGF scheme.[18] In order to minimize the required memory and reduce the computational burden, only the diagonal part of scattering self-energies has been taken into consideration. There is no clear physical justification for this approximation but it appeared to be the only way to treat realistic three-dimensional nanostructures.

In this paper we present a basis expansion method to overcome the above computational limitations without losing essential physics of quantum transport in NWs. We consider a nonequilibrium steady state of a NW device as a result of scattering processes in a reference ideal wire. A periodic Hamiltonian of this wire yields a spectrum of one-particle Bloch states and describes free mobile carriers in the device. The rest of the device Hamiltonian represents various scattering mechanisms including electric field and interaction of the mobile carriers with their environment (impurities, lattice vibrations, etc). Under normal bias conditions, the electronic transport is dominated by the free carriers at the bottom of the allowed band of the wire, and the steady states can be calculated, at least in principle, as a mixture of the Bloch states in a narrow energy interval. Our purpose will be to construct a moderate representative basis which reproduces all the scattering states within the energy interval of interest. Neglecting contribution outside this energy range, we replace the original huge set of the atomic orbitals with the new basis and obtain a low-dimensional equivalent model in the basis representation.

The basis expansion is commonly used in the effective mass model. In the mode space approach, scattering wave functions $\Psi(\boldsymbol{r}) = \sum_\nu \Phi_\nu(\boldsymbol{\sigma})\xi_\nu(x)$ are represented by the subband bound states Φ_ν in the wire cross section. The three-dimensional transport problem is thus reduced to a much easier task of computing a few one-dimensional functions $\xi_\nu(x)$ in the transport direction. The subband eigenstates coincide up to a phase factor with the Bloch states $\Psi_\nu(\boldsymbol{r} + \boldsymbol{e}_x\Delta x) = \Psi_\nu(\boldsymbol{r})\exp(ik_\nu\Delta x)$ in an ideal wire with parabolic band structure. Thus, the mode space approach seems to allow for a direct generalization to atomistic Hamiltonians. Although the local two-dimensional quantization cannot be performed in this case, one can always calculate enough Bloch states within the energy interval of interest and extract a reduced basis which suffices to reproduce all these states with enough accuracy. We see below that such a simple procedure generally fails. The main difficulty comes from the fact that the device Hamiltonian is no longer a bounded operator. As a result, there is no energy minimization principle to guarantee correct spectrum of the basis-transformed model even if the basis reproduces well all the physical states of interest. The failure of the ordinary variational procedure shows up clearly in the erroneous band structure of the model and this problem deserves special treatment.

In the next section, we introduce necessary definitions, construct a representative basis of Bloch states and discuss the unphysical band structure of the reduced model in the basis representation. This problem is solved in Sec. III, where we formulate a variation method to deal with an arbitrary part of spectra of the Bloch Hamiltonians. The method converts the primary basis of Bloch states into a new one with correct physical properties. The low-dimensional equivalent transport model (EM) is obtained by the basis transformation of the tight-binding device Hamiltonian with scattering terms incorporated. Section IV demonstrates application of EMs to various SiNWFETs in ballistic and nonballistic regimes. Section V gives concluding remarks.

II. BASIS REPRESENTATION IN QUANTUM WIRE

We consider an ideal wire with the tridiagonal block Hamiltonian (see Fig. 1),

$$H_{nn} = H_0; \quad H_{n\,n+1} = H^T_{n+1\,n} = W, \tag{1}$$

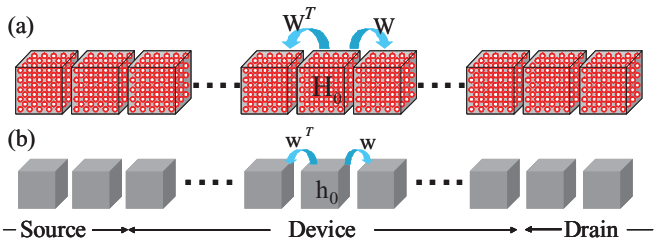

FIG. 1. (Color online) Schematic diagram of an ideal wire with tridiagonal block Hamiltonian (a) in the original tight-binding picture [Eq. (1)] and (b) in the basis representation [Eq. (6)]. An interaction Hamiltonian is introduced into the central part (device area) after constructing the basis representation.

where n is the number of unit structures in the ideal wire, H_0 is the tight-binding Hamiltonian for an isolated unit structure, and W contains coupling terms between the atomic orbitals in two neighboring unit structures. The size of blocks N_{TBM} is the number of atomic orbitals in one unit structure which depends on the lattice orientation and the tight-binding method (TBM).

The scattering states of the ideal wire are in the form $\Psi_n = e^{iqn}\Theta(q)$, where N_{TBM} possible Bloch states are found from the Hermitian eigenvalue problem

$$H(q)\Theta_\nu(q) \equiv [H_0 + We^{iq} + W^T e^{-iq}]\Theta_\nu(q) = \varepsilon_\nu(q)\Theta_\nu(q). \tag{2}$$

We are interested in a relatively narrow energy interval $[\varepsilon_1;\varepsilon_2]$ such that the number of subbands with energies $\varepsilon_\nu(q) \in [\varepsilon_1;\varepsilon_2]$ is much smaller compared to N_{TBM}. A smooth q dependence of the subband energies suggests that one can use the Bloch states $\Theta_\nu(q)$ at few representative wave numbers to construct an appropriate basis for all other states within the energy interval of interest. An alternative way is to solve the Bloch eigenvalue problem,[30]

$$[W^T Z^{-1} + H_0 + WZ - \varepsilon]\Theta = 0, \tag{3}$$

at few representative energies ε and retain the scattering eigenstates $(\Theta_\nu(\varepsilon), Z_\nu(\varepsilon))$ with $|Z_\nu| = 1$. More generally, one can consider an arbitrary set of points (q_i,ε_i) in various subbands which "represent" well enough all the branches of the band structure within $[\varepsilon_1;\varepsilon_2]$. It is hardly possible to formulate the best algorithm of how to choose the representative states in a generic band structure. However, this is never a problem in practice, since, as we will see, the basis can be tested and improved in the course of the construction. For a moment, let us just assume a set of properly chosen Bloch states Θ_i associated with points (q_i,ε_i) in the band structure with $\varepsilon_i \in [\varepsilon_1;\varepsilon_2]$. Figure 2(a) shows an example: the Bloch states in a thin p-SiNW at two reference energies -0.3 and -0.4 eV

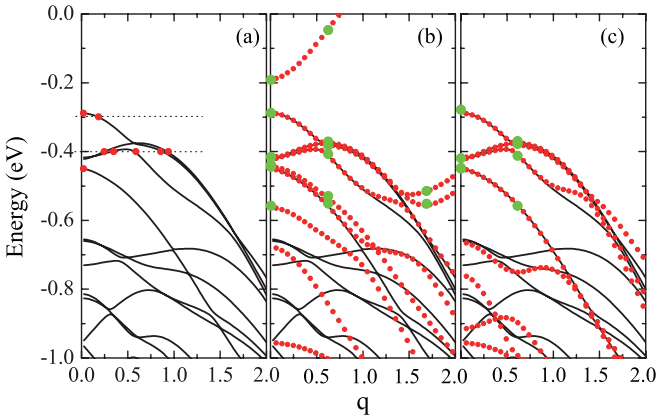

FIG. 2. (Color online) Constructing EM basis in a [100] p-SiNW with rectangular cross section 2.2 × 2.2 nm. (a) Band structure near the top of the valence band. The red points show the representative Bloch states. (b) Band structure of the primitive reduced model with artificial unphysical branches. The green points of larger size indicate the subband energies $\varepsilon_\nu(q) \in [-0.6;0]$ (eV) at three wave numbers $q = 0, 0.6$, and 1.7. The variational method is designed as to minimize the number of these points. (c) The band structure after eliminating the unphysical branches.

are expected to reproduce the spectrum at the top of the valence band. Two more states at $q = 0$ are added in order to ensure exact valence band edge and incorporate the next subband threshold at ~ -0.44 eV. The representative Bloch states can be further transformed into a real-valued orthogonal basis set. The real and imaginary parts of the Bloch states are taken as M columns of a $N_{\mathrm{TBM}} \times M$ real matrix $\widetilde{\Phi}$. In the case of Fig. 2(a), there are six states at $q \neq 0$ and two more states at $q = 0$ giving $M = 14$ real functions in total. After diagonalizing the overlap matrix $\tilde{\Phi}^T \tilde{\Phi} = c \Lambda c^T$, we obtain the matrix with orthonormal columns

$$\Phi = \widetilde{\Phi} c \Lambda^{-1/2}; \quad \Phi^T \Phi = 1 \tag{4}$$

for the basis representation

$$\Theta_\nu(q) = \Phi \theta_\nu(q). \tag{5}$$

Hereafter we employ matrix notations and omit the indices for the atomic orbitals and the basis states. To make a distinction with the original tight-binding model, the quantities in the basis representation are denoted using lowercase letters. The basis size N_b (i.e., the number of columns in Φ and the length of array θ_ν) is generally less than M since the initial functions can be linearly dependent and the corresponding eigenstates of the overlap matrix with numerically small Λ_i should be eliminated. By the construction, the basis representation Eq. (5) is exact for the Bloch states at the representative points (q_i, ε_i) and it shows fairly good agreement for all other states in the considered energy interval. Inserting Eq. (5) into Eq. (2) or Eq. (3) and premultiplying by Φ^T, one obtains the equations in the basis representation with the $N_b \times N_b$ model Hamiltonian

$$h_{nn} = h_0 = \Phi^T H_0 \Phi; \quad h_{nn+1} = h^T_{n+1n} = w = \Phi^T W \Phi. \tag{6}$$

The accuracy of Eq. (5) can be estimated from the band structure in this basis-transformed model. Lack of accuracy around some $\varepsilon_\nu(q)$ would indicate that the corresponding Bloch state should be added into the basis. Repeating the orthogonalization, one obtains a new basis with better accuracy.

Extra scattering terms Σ_{nm} in the open device Hamiltonian mix the free states $e^{iqn}\Theta_\nu(q)$ and bring about the formation of a nonequilibrium device state $\Psi_n = \sum_{\nu,q} \Theta_\nu(q) C_{n\nu}(q)$. Assuming the validity of Eq. (5) for all relevant Bloch states, we obtain

$$\Psi_n = \Phi \psi_n, \tag{7}$$

where ψ_n is a nonequilibrium state in the model Hamiltonian Eq. (6) plus the basis-transformed scattering terms $\Phi^T \Sigma_{nm} \Phi$. Compared to the original tight-binding model, the size of the device Hamiltonian is reduced by a factor of $N_b/N_{\mathrm{TBM}} \ll 1$, which greatly facilitates the transport simulations.

The above procedure is straightforward and fairly simple but the reduced model with so-obtained basis generally fails. It turns out that the accurate basis representation of the Bloch states Eq. (5) is a necessary but not a sufficient condition for constructing a model with correct physical properties. This becomes apparent by looking at the band structure of the model Eq. (6). Figure 2(b) shows an example. By the construction, the model Hamiltonian does reproduce physical subband but it also allows for unphysical scattering states within the same energy interval which makes the model useless because of the erroneous density of states. This kind of problem could be anticipated: In any basis expansion method, the basis transformed model Hamiltonian contains both physical and unphysical levels. For a bounded Hamiltonian operator, the unphysical states have higher energies and can be disregarded. This is not the case for a realistic band structure with both valence and conduction bands.

The problem of extracting a sensible basis from a group of energy bands has been studied previously in the context of Wannier functions (WFs) which have recently found important applications in electronic structure calculations. The method of maximally localized (maxloc) WFs has been developed to perform practical calculations of the minimal basis set.[31–33] The maxloc WFs have been successfully used in the first-principles study of bulk dielectric properties of insulators[34] and quantum transport in atomic chains.[35] In the present case, however, we need to reproduce N_{TBM}-component Bloch states $\Theta_\nu(q)$ with strong dispersion across the one-dimensional Brillouin zone. Each $\Theta_\nu(q)$ generally has noticeable overlap with a large number of states in both valence and conduction bands at different q. In such case, constructing the Wannier representation is not much help since the corresponding Hamiltonian would contain a long-range interaction part.

In order to obtain a correct physical model with a short-range Hamiltonian [Eq. (6)], we have developed a variational method which enables unphysical part of the spectrum to be eliminated. Let Φ be a $N_{\mathrm{TBM}} \times N_b$ basis matrix which reproduces all the Bloch states within $[\varepsilon_1; \varepsilon_2]$. The band structure of the corresponding reduced model is obtained from the $N_b \times N_b$ Bloch Hamiltonian

$$h(q) = \Phi^T H(q) \Phi. \tag{8}$$

Many of its eigenstates do not correspond to any physical solution but may easily fall within $[\varepsilon_1; \varepsilon_2]$, giving rise to the unphysical subbands of the model. Let us consider an extra basis state ($N_{\mathrm{TBM}} \times 1$ real array) $\widetilde{\Phi} : \Phi^T \widetilde{\Phi} = 0$ and define a new model with basis $\Phi \otimes \widetilde{\Phi}$. The corresponding $(N_b + 1) \times (N_b + 1)$ Bloch Hamiltonian reads

$$\widetilde{h}(q) = \begin{vmatrix} h(q) & X(q) \\ X^\dagger(q) & H_{\widetilde{\Phi}\widetilde{\Phi}}(q) \end{vmatrix}, \tag{9}$$

where the $N_b \times 1$ array $X(q)$ is given by

$$X(q) = \Phi^T H(q) \widetilde{\Phi}. \tag{10}$$

Adding an extra basis state does not deteriorate the basis expansion Eq. (5) and has no effect on the physical subbands but the rest of the model band structure may strongly depend on $\widetilde{\Phi}$. Our purpose is to find a new model with fewer branches within $[\varepsilon_1; \varepsilon_2]$ compared to the previous one. We construct an analytical functional $F[\widetilde{\Phi}]$ which returns lower values for models with fewer subbands in this energy interval. The physical model with correct band structure is the one where $F[\widetilde{\Phi}]$ takes its minimum value. Hence, constructing this model can be turned into a variational problem.

III. CONSTRUCTING EQUIVALENT MODEL

We introduce a function of energy,

$$N(\varepsilon) = \left\langle \frac{z-\varepsilon_c}{z-\varepsilon} \right\rangle \equiv \frac{1}{2n_z} \sum_{k=1}^{2n_z} \frac{z_k - \varepsilon_c}{z_k - \varepsilon}, \tag{11}$$

where $\varepsilon_c = (\varepsilon_1 + \varepsilon_2)/2$ and $z_k = \varepsilon_c + \rho e^{\frac{i\pi}{n_z}(k-\frac{1}{2})}$ are $2n_z$ points in the complex z plane along the contour C with center ε_c and radius $\rho = (\varepsilon_2 - \varepsilon_1)/2$. For brevity's sake, we drop the constant parameters $\varepsilon_{1,2}$, n_z in $N(\varepsilon)$. One can readily check that (1) $N(\varepsilon)$ is a real-valued analytical function for all real ε; (2) $N(\varepsilon)$ is symmetric with respect to ε_c, where it reaches its maximum value; and (3) n the limit of large n_z, $N(\varepsilon) = \frac{1}{2\pi i} \oint_C \frac{dz}{z-\varepsilon} + O(\frac{1}{n_z})$ returns 1 or 0 depending on whether ε is inside or outside the energy interval $[\varepsilon_1; \varepsilon_2]$. $N(\varepsilon)$ can be thought as a contribution to the "number of states" within $[\varepsilon_1; \varepsilon_2]$ from a single energy level ε. The smoothness of thus defined "number of states" is controlled by n_z.

Let ε be an unphysical level in a model with a trial basis state $\widetilde{\Phi}$ and let $[\varepsilon_1; \varepsilon_2]$ be the energy interval where we need the model to be correct. The "number of states" becomes an analytical functional $N(\varepsilon[\widetilde{\Phi}])$ which gives ~ 1 for $\varepsilon \in [\varepsilon_1; \varepsilon_2]$ and $\ll 1$ for $\varepsilon \notin [\varepsilon_1; \varepsilon_2]$. Thus, minimization of $N(\varepsilon[\widetilde{\Phi}])$ solves the problem of eliminating this unphysical level from $[\varepsilon_1; \varepsilon_2]$.

Generalization to a model band structure is straightforward. We introduce the variational functional

$$F[\widetilde{\Phi}] \equiv \sum_{i=1}^{n_q} \sum_{\nu} N(\varepsilon_\nu(q_i, [\widetilde{\Phi}])), \tag{12}$$

which gives the total "number of states" at n_q representative wave numbers q_i. Figure 2(b) illustrates our construction. In this particular example we set $\varepsilon_1 = -0.6\,\text{eV}$, $\varepsilon_2 = 0\,\text{eV}$ and consider three wave numbers $q = 0$, 0.6, and 1.7. The branch index ν in Eq. (12) runs over all the subbands, but the main contribution comes from the terms $\varepsilon_\nu(q_i) \in [\varepsilon_1; \varepsilon_2]$ shown in Fig. 2(b) by the green points of larger size. Minimization of the variational functional Eq. (12) shifts the unphysical points away from $[\varepsilon_1; \varepsilon_2]$ and yields a model with correct band structure [Fig. 2(c)].

Inserting Eq. (11) into Eq. (12), we obtain

$$F[\widetilde{\Phi}] = \left\langle \sum_i \mathrm{Tr} \left[\frac{1}{z - \widetilde{h}(q_i)} \right] (z - \epsilon_c) \right\rangle, \tag{13}$$

where $\widetilde{h}(q)$ is given by Eq. (9) and $\langle \cdots \rangle$ is defined in Eq. (11). Calculating the trace of the resolvent, we arrive at

$$F[\widetilde{\Phi}] = F_0 + \Delta F[\widetilde{\Phi}], \tag{14}$$

where F_0 is the "number of states" in the original model without $\widetilde{\Phi}$ and

$$\Delta F[\widetilde{\Phi}] = \left\langle \sum_i \frac{1 + X^\dagger(q)(z - h(q_i))^{-2} X(q)}{z - H_{\widetilde{\Phi}\widetilde{\Phi}}(q) - X^\dagger(q)(z - h(q))^{-1} X(q)} (z - \epsilon_c) \right\rangle \tag{15}$$

"measures" changes in the unphysical part of the band structure. A minimum value $\Delta F[\widetilde{\Phi}_{\min}] \sim -n_q$ is reached in the new model $\Phi \times \widetilde{\Phi}_{\min}$ with one unphysical branch eliminated.

In practice, we calculate $\widetilde{\Phi}$ in the form

$$\widetilde{\Phi} = \frac{1}{\sqrt{C^T C}} \Xi C, \tag{16}$$

where C is an array of M' expansion coefficients and the $N_{\text{TBM}} \times M'$ trial basis matrix Ξ will be shortly discussed later. Inserting Eq. (16) in Eq. (15), we obtain the rational variational function

$$\Delta F(C) = \frac{1}{2n_z} \sum_{i=1}^{n_q} \sum_{k=1}^{2n_z} \frac{C^T A(q_i, z_k) C}{C^T B(q_i, z_k) C} (z_k - \varepsilon_c) + (C^T C - 1)^2, \tag{17}$$

where A, B are given by

$$A(q,z) = 1_{M' \times M'} + \Xi^T H(q) \Phi [z - h(q)]^{-2} \Phi^T H(q) \Xi, \tag{18}$$

$$B(q,z) = z 1_{M' \times M'} - \Xi^T H(q) \Xi - \Xi^T H(q) \Phi [z - h(q)]^{-1} \Phi^T H(q) \Xi, \tag{19}$$

and the last term has been added for numerical reasons. Note that the coefficients in the trial basis expansion [Eq. (16)] are not normalized so that we can perform an unconstrained minimization. The variational functional is invariant with respect to transformation $C \to \alpha C$, which causes convergence problems. The last term in Eq. (17) breaks this symmetry and ensures fast convergence.

We have thus reduced the problem to minimization of a rational analytical function $\Delta F(C)$. To complete the construction, the trial basis Ξ still needs to be specified. In practice, we orthogonalize the columns of the primary $N_{\text{TBM}} \times 2N_b$ matrix

$$[(1 - \Phi\Phi^T) H_0 \Phi,\ (1 - \Phi\Phi^T)(W + W^T)\Phi] \tag{20}$$

and obtain $M' \leqslant 2N_b$ basis functions Ξ. Here $(1 - \Phi\Phi^T)$ acts as a projector to the orthogonal complement to the functional space of the unphysical model, and Ξ includes all the functions with nonzero matrix elements $\Xi_i^T H(q) \Phi_j$ for $q = 0$ and $q = \pi$. This choice of Ξ is certainly not unique. For example, one can enlarge the trial basis by postulating nonzero matrix elements with W and W^T separately or even use the full $(N_{\text{TBM}} - N_b)$-dimensional orthogonal complement. However, numerical tests show that a larger variational space is not needed. By the construction, the above trial basis offers enough freedom to eliminate unphysical energies at $q = 0$ and $q = \pi$, which suffice to guarantee correct band structure at all q. For the same reason, there is generally no need for many representative wave numbers in the variational functional Eq. (12). Even $n_q = 2$ with $q_i = 0$, π already gives a stable variational scheme. In most of the calculations below we used $n_q = 3$ with $q_i = 0$, $\frac{\pi}{2}$ and π.

Let us now summarize the variational procedure. First of all, one must specify the energy interval which needs to be reproduced by the equivalent model. The choice depends on the problem at hand. For atomistic transport in MOSFETs, a good strategy would be to start with a small EM which reproduces a few lowest branches in the allowed band and

a certain part of the forbidden band in order to prevent an unphysical leakage current. For a given interval $[\varepsilon_1;\varepsilon_2]$, the calculations proceed as follows.

(1) Choose a number of representative points in the band structure and calculate the corresponding Bloch states. Construct the primary basis Eq. (4) and calculate the band structure in the corresponding reduced model Eq. (6). Make sure that the band structure contains all the physical branches within the energy interval of interest. Otherwise, add necessary Bloch states and recalculate the basis.

(2) Given an N_b-dimensional model, orthogonalize $2N_b$ columns in Eq. (20) and obtain the trial basis Ξ.

(3) Compute necessary matrix elements which define A, B in Eqs. (18) and (19). The variational functional depends of two integer parameters. $n_z = 3$ and $n_q = 3$ ($q_{1-3} = 0, \frac{\pi}{2}, \pi$) is a good choice.

(4) Minimize ΔF and obtain the new basis state $\widetilde{\Phi}_{\min}$ Eq. (16). Since both the function and its derivatives are calculated analytically, one can effectively use any available method for unconstrained minimization. The simulations below employ the conjugate gradient method. The basis $\Phi \otimes \widetilde{\Phi}_{\min}$ defines a new (N_b+1)-dimensional model with fewer unphysical branches. If there are still unphysical branches in the new model, return to (2) and repeat. Generally, it is difficult to eliminate more than one unphysical branch in one step.

The trial basis Eq. (16) does not distinguish between different unphysical branches and the result of minimization depends on the initial $\widetilde{\Phi}$. One may consider a slightly different trial basis in order to specify the branch to be eliminated. For example, using the null space of $\sum_{\nu\neq\nu_0}(1-\Phi\Phi^T)H(q_0)\Phi\theta_\nu(q_0)\theta_\nu^\dagger(q_0)\Phi^T H^\dagger(q_0)(1-\Phi\Phi^T)$ instead of the full orthogonal complement, one obtains a smaller trial basis which is effective in removing the branch where $\varepsilon_{\nu_0}(q_0)$ belongs. Which basis to use is a matter of choice; both give similar performance. The variational simulations are very fast: CPU time for items (2)–(4) in the above scheme is negligible compared to computing the representative Bloch states in item 1.

In the above example, a 17-dimensional model with correct band structure at the top of the valence band [Fig. 2(c)] is obtained from the one in Fig. 2(b) by successive variational calculations of three supplementary basis states. This basis can be further used as a good starting point to construct EMs with wider band structures. Just add extra Bloch states from the missing part of the desired energy range [the last sentence before (2)] and proceed as before. In this way, we have obtained the larger 36D, 46D, and 53D EMs shown in Fig. 3. Hereafter, we use the notation N_bD EM for a model with N_b basis states per unit structure. In transport simulations, one should choose appropriate EMs in order to optimize computer performance and ensure accurate results.

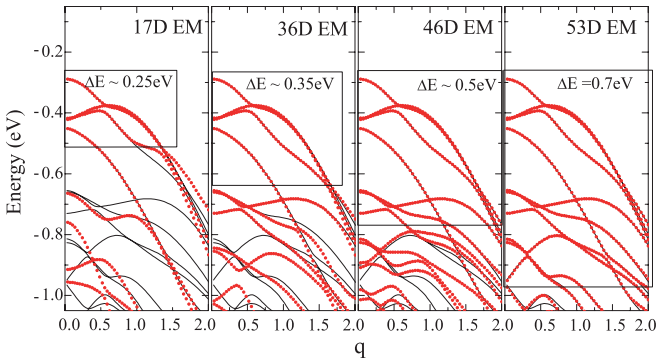

FIG. 3. (Color online) EMs in a p-Si NW along [100] crystal axis with a rectangular cross section 2.2 × 2.2 nm. The black lines show the band structure in the sp^3s^* tight-binding model. The red points represent four EMs with $N_b = 17$, 36, 46, and 53. ΔE is the energy window reproduced by the EMs.

IV. EM IN ATOMISTIC TRANSPORT SIMULATIONS

The structure of the SiNWFETs used in our simulations is depicted in Fig. 4. We consider NWs with $d = 2.2$, 3, and 4 nm along three main crystal directions. Other parameters are $V_{SD} = 0.1$ V, $T = 300$ K, $\epsilon_{Si} = 11.9$, $\epsilon_{SiO_2} = 3.8$, $t_{ox} = 1$ nm, dopant concentration in the source/drain regions is 10^{20} cm^{-3} for n-Si and 2×10^{19} cm^{-3} for p-Si NWs. The length of the wire is adjusted in order to have N blocks in the device, the first (source) and the last (drain) blocks are used to form two semi-infinite leads connected to equilibrium reservoir with different Fermi levels $\mu_R = \mu_L - eV_{SD}$. The source Fermi level μ_L is fixed by the condition of zero average total charge in the corresponding ideal wire. The low-dimensional device Hamiltonian is obtained by the basis transformation. In the ballistic regime, the one-particle Hamiltonian h is given by Eq. (6) plus the basis-transformed potential term. More generally, we perform the basis transformation in the second quantization picture,

$$C = \hat{\Phi}c, \quad C^\dagger = \hat{\Phi}c^\dagger, \tag{21}$$

where C, $C^\dagger$, and $(c,\ c^\dagger)$ are the arrays of the TBM (EM) annihilation/creation operators in the entire device and $\hat{\Phi}$ is the block diagonal matrix with N diagonal elements Φ. These notations should not be confused with the expansion coefficients in the previous section. The corresponding relation between the NEGFs reads

$$G^{R,A,>,<} = \hat{\Phi} g^{R,A,>,<} \hat{\Phi}^T, \tag{22}$$

and $g^{R,A,>,<}$ are to be obtained by solving the standard NEGF equation,[20,21]

$$g^R(\varepsilon) = \left(\varepsilon - h - \sigma_{ph}^R - \sigma_c^R\right)^{-1};\ g^A = g^{R\dagger}, \tag{23}$$

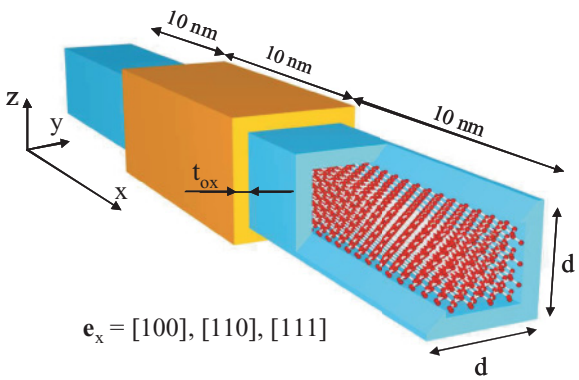

FIG. 4. (Color online) GAA SiNWFETs used in the simulations.

$$g^{\gtrless}(\varepsilon) = g^{R}(\varepsilon)\left(\sigma_{\rm ph}^{\gtrless}(\varepsilon) + \sigma_{c}^{\gtrless}(\varepsilon)\right)g^{A}(\varepsilon), \qquad (24)$$

in the EM picture. The contact self-energies in two boundary blocks are calculated as[30]

$$\sigma_{cN}^{R} = w\,\overrightarrow{\chi}_{R}\,\overrightarrow{z}_{R}\,\overrightarrow{\chi}_{R}^{-1}; \quad \sigma_{c1}^{R} = w^{T}\,\overrightarrow{\chi}_{L}\,\overrightarrow{z}_{L}\,\overrightarrow{\chi}_{L}^{-1}, \qquad (25)$$

where $\overrightarrow{\chi}_{L,R}$, $\overrightarrow{z}_{L,R}$ are the matrices of the outgoing/decaying Bloch states and the Bloch factors in the corresponding (left or right) leads. These states are obtained from the eigenvalue problem akin to Eq. (3) with H_0, W replaced with appropriate $N_b \times N_b$ blocks of the EM Hamiltonian. $\sigma_c^{\gtrless}(\varepsilon)$ at each contact are given by the fluctuation dissipation theorem.[21] The electron-phonon terms $\sigma_{\rm ph}$ are discussed below.

The NEGF equations in the EM picture do not involve any large quantities and can be solved easily. The electric current is calculated directly from $g^{\gtrless}$, $\sigma_c^{\gtrless}$ without referring to the tight-binging model. In self-consistent transport simulations, the Poisson equation for the device electrostatics includes atomistic distribution of the mobile charge. In the ballistic regime, we use the R-matrix technique[24–26] and calculate the charge as a sum of partial contributions from separate scattering states. N_b-dimensional unit structures of the EM model are used as the "atoms" in the R-matrix propagation scheme.[26] After transforming scattering states back to the tight-binding picture [Eq. (7)], the mobile charge at separate atoms can be calculated. In the general case, we use Eq. (22) to calculate diagonal elements of the lesser/bigger Green's functions, which never causes any time or storage problems.

A. Ballistic regime

Our first example is ballistic transport in a [100] p-SiNWFET with $d = 2.2$ nm in the scope of the sp^3s^* tight-binding model. Four different EMs for this NW have been constructed in the previous section (see Fig. 3). The smallest EM is used to perform fast preliminary self-consistent transport calculations. In this case, computing device state at each realization of the electrostatic potential takes seconds

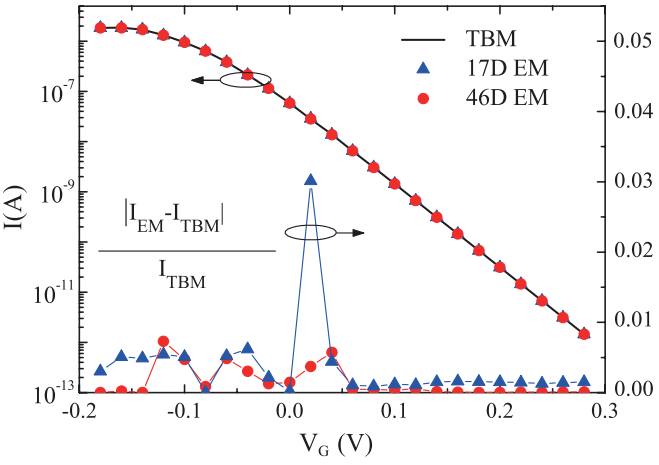

FIG. 5. (Color online) I-V characteristics of a p-SiNW FET with $d = 2.2$ nm. The transport direction is aligned with the [100] crystal axis. The solid line is the exact TBM results. The points represents two EMs from Fig. 3. The lower part of the figure shows the relative error in the self-consistent EM calculations.

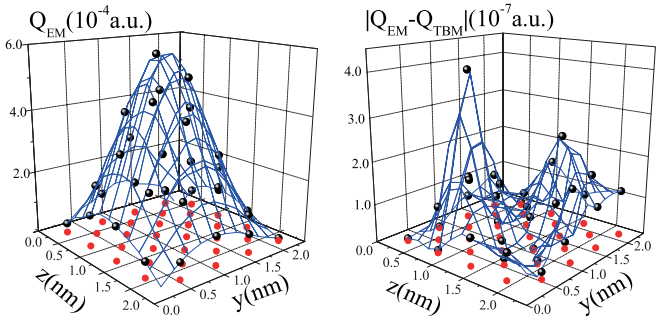

FIG. 6. (Color online) An example of the mobile charge distribution in one atomic layer of a p-SiNW. The left panel shows the atomistic mobile charge in the 17D EM. The red points indicate positions of 32 Si atoms in the wire cross section. The right panel presents the absolute error of EM data.

on a 2.7-GHz workstation. The calculations are repeated with larger EMs in order to check convergence and estimate the accuracy of the computed drain current. Figure 5 presents our results. The transport characteristics in two EMs are compared with the exact TBM data. The lower part of the figure shows the relative error in the EM calculations. The difference between three I-V curves is $\sim$1% which is within the level of convergence of the self-consistent calculations. In this sense, the results are identical. We have also confirmed that even in the smallest 17D EM, both the amplitude and the phase of the scattering wave functions in the basis representation reproduce the exact solutions at individual atomic orbitals. As an illustration, we show in Fig. 6 the charge distribution in the device steady state at $V_G = -0.1$ V in one atomic layer near the source contact. The right panel of the figure presents the absolute error. The figure clearly demonstrates that the model indeed reproduces atomistic details of the device state which explains the high accuracy of the EM transport calculations. The reliable energy interval ΔE in the EM band structure is the main criterion which controls the transport model. At the present bias conditions, $\Delta E \sim 0.25$ eV is likely to be enough for accurate simulations.

We next consider ballistic transport in various n-SiNW FETs in Fig. 4 using the $sp^3d^5s^*$ tight-binding model. The largest TBM device Hamiltonian is for the 4×4-nm NWs along the [111] directions (248 960 orbitals). Even in the ballistic regime, transport simulations in these devices can be rather challenging and there is no way for modeling inelastic effects with our present computer resources. The problem is eliminated by using the EMs. Again, we construct a set of EMs for each device and use the cheapest model to perform a major part of the self-consistent simulations. The EMs with wider band structure are further used to test and improve the accuracy. Figure 7 presents the conduction band structure in three NWs with $d = 4$ nm (solid lines). The top panel also shows geometry of the unit structures and the corresponding number of atomic orbitals $N_{\rm TBM}$. The red points are for the band structure in the largest constructed EMs. The energy range up to $\sim$1.55 eV can be reproduced by using $\sim$1%–2% of all the atomic orbitals which greatly reduces the computational burden. Moreover, we do not actually need all the subbands in Fig. 7 to obtain accurate transport characteristics. An $\sim$1 % level of accuracy is achieved with twice smaller EMs. Figure 8

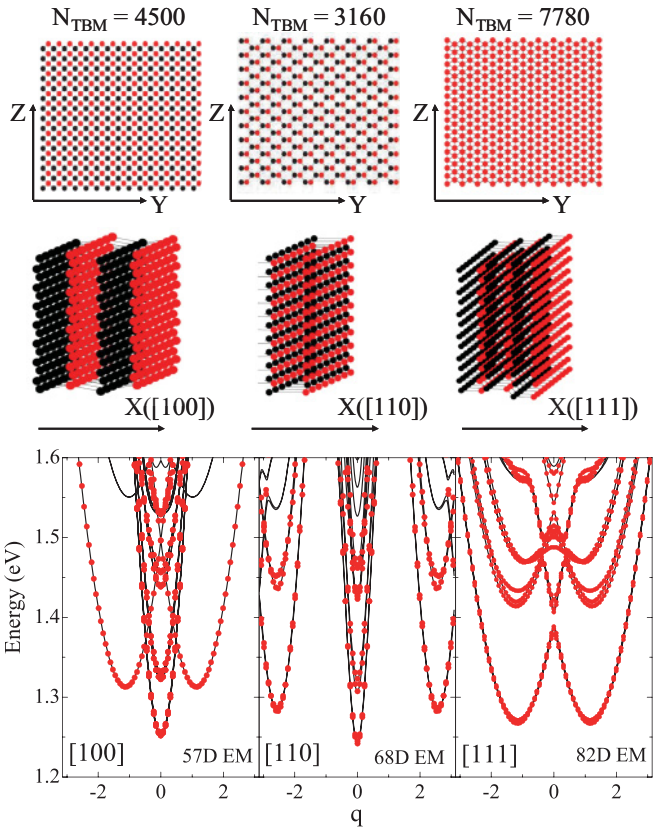

FIG. 7. (Color online) Conduction band in n-SiNWs with $d = 4$ nm along the [100], [110], and [111] crystal directions. The red points represent the largest EMs with $N_b = 57, 68, 82$, respectively. The top panel shows the geometry of the NW unit structures with N_{TBM} atomic orbitals.

presents our results. The subthreshold swing in these nine devices has been estimated as 67, 75, 84 for [100] NWs, 66, 75, 88 for [111] NWs, and 72, 77, 87 for [110] NWs (all in mV/dec); smaller values are for thinner NWs. For the largest 4×4-nm [111] NWFET, computing the I-V curve with $\sim$1% accuracy takes a few hours. These results are obtained with the 46D EM shown in Fig. 9 together with two other EMs. The smallest 30D EM in this figure is constructed so as to reproduce the lowest bunch of six nearly degenerate branches in the

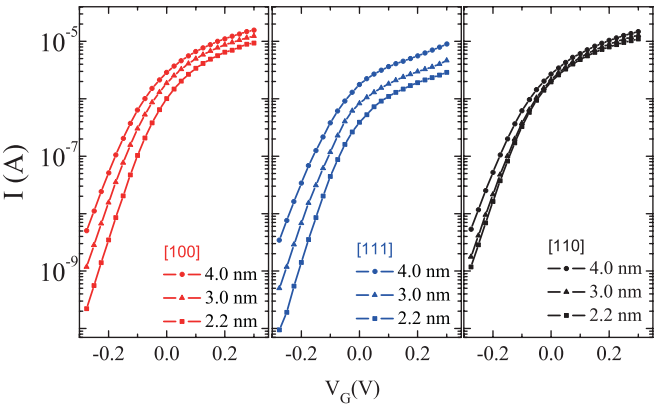

FIG. 8. (Color online) I-V characteristics of n-SiNWFETs in Fig. 4 with $d = 2.2$, 3, and 4 nm.

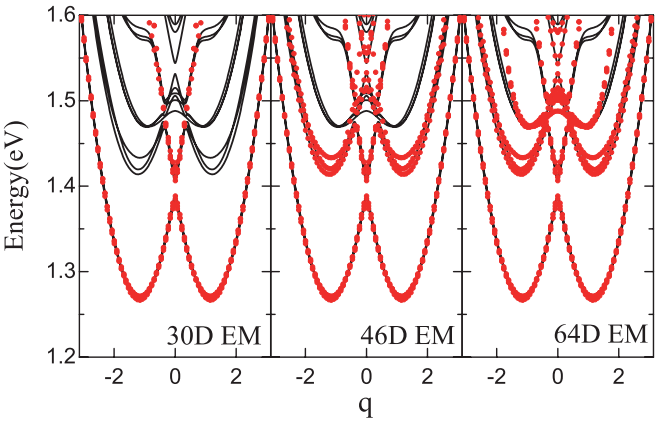

FIG. 9. (Color online) The conduction band in three EMs ($N_b = 30$, 46, and 64) for a [111] n-SiNW with $d = 4$ nm.

conduction band of Si. The 46D EM includes the next bunch of six subbands and so on. The sequence of the EMs in Fig. 9 is reminiscent of the mode space approach in the effective mass picture with different number of subbands taken into consideration. In this sense, the lowest 30D EM is an analog of the one-dimensional approximation in the continuous model.

Figure 10 illustrates convergence of the EM simulations. Even the simplest EM provides reasonable estimates for the drain current. Approximately 5% accuracy in this model is what could be expected from our experience with the mode space approach. Including the next bunch of subbands (46D EM) yields convergent results which can hardly be distinguished by eye from the 64D EM. Note that, similar to our previous example, $\Delta E \sim 0.2$ eV seems to ensure enough accuracy at the present bias conditions. Similar accuracy was confirmed for other devices.

B. Electron-phonon scattering

Studying quantum transport in the presence of electron-phonon coupling is much more complex. Full Green's functions and self-energies need to be computed and stored at many energies. For realistic devices, such full-scale atomistic NEGF simulations simply cannot be done, not even by running

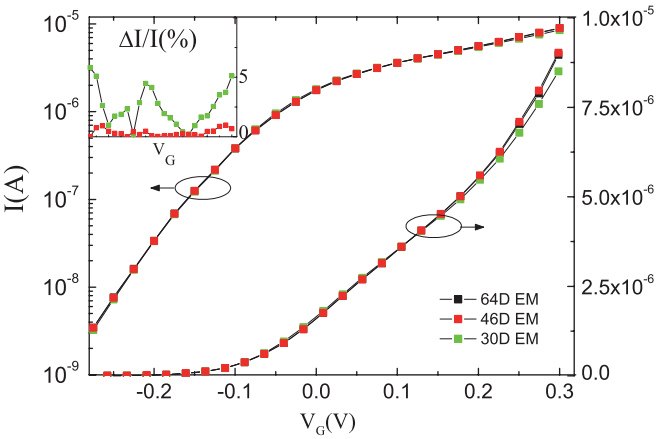

FIG. 10. (Color online) Convergence of I-V function in EMs from Fig. 9. The inset shows the relative difference with the largest 64D EM.

highly parallelized computer codes on hundreds of cores. Using equivalent models of small size offers a promising way around this problem by reducing the computational time and memory by factors of $(N_b/N_{\rm TBM})^3$ and $(N_b/N_{\rm TBM})^2$, respectively. The above examples have demonstrated that one can use only $N_b/N_{\rm TBM} \sim 1\%$ of all the atomic orbitals and reproduce the device physics in the ballistic regime. Here we address the question on how the inelastic terms affect the accuracy and convergence of the EMs. The main effect of the electron-phonon scattering on the transport properties of NWFETs comes from enhanced backscattering which reduces the drain current and changes electrostatics in the source region. Since the inelastic scattering processes mix electronic states at different energies, accurate studies of nonballistic transport may need wider band structure compared to the ballistic calculations. This is especially so for the OFF states with steep potential change in the gate region where the backscattering is most important.

We have calculated the electron-phonon scattering in the p-SiNWFET from our first example. In order to construct the inelastic self-energy terms $\sigma_{\rm ph}^{R,>,<}$, it is convenient to use global numeration of the atomic orbital instead of the block matrix notation. The electron-phonon coupling is introduced by assuming the coordinate-dependent TBM matrix elements $T_{ij}(|\boldsymbol{R}_i - \boldsymbol{R}_j|)$, where i, j are the numbers of individual atomic orbitals and $\boldsymbol{R}_{i,j}$ stand for the positions of the corresponding atoms. Without phonons, the atoms are fixed $\boldsymbol{R}_i = \boldsymbol{R}_{i0}$ and the matrix elements $T_{ij}^0 \equiv T_{ij}(|\boldsymbol{R}_{i0} - \boldsymbol{R}_{j0}|)$ define the tight-binding Hamiltonian for ballistic transport. The lattice vibrations $\boldsymbol{R}_i = \boldsymbol{R}_{i0} + \boldsymbol{u}_i(t)$ give rise to the electron-phonon interaction term

$$H_{\text{e-ph}} = \sum_{ij} \delta T_{ij} C_i^+ C_j, \tag{26}$$

where i, j run over all pairs of orbitals at two nearest neighbors. Generally, it would be necessary to solve a separate eigenvalue problem for the lattice vibrations in order to obtain the electron-phonon Hamiltonian with quantized phonon modes.[18,36,37] In this work, we skip this part and restrict our consideration to a simple physical model which suffices to test the EMs. We assume $T_{ij} \sim 1/(\boldsymbol{R}_i - \boldsymbol{R}_j)^2$ and consider quasi-one-dimensional phonon modes $\boldsymbol{u}_i = \boldsymbol{e}_x u_i$ in the [100] direction. In the lowest order $\delta T \sim u$ we obtain

$$\delta T_{ij} = 2T_{ij}^0 \frac{(\boldsymbol{R}_{j0} - \boldsymbol{R}_{i0})_x}{(\boldsymbol{R}_{i0} - \boldsymbol{R}_{j0})^2}(u_i - u_j) \equiv \tilde{T}_{ij}(u_i - u_j), \tag{27}$$

where $\tilde{T}_{ij} = \pm\frac{8}{3a_0}T_{ij}^0$ and $a_0 = 0.5431$ nm is the lattice constant. The longitudinal phonon modes are approximated by ($\hbar = 1$)

$$u_i \equiv u_{aL} = \sum_{q,\lambda} \frac{f_{a\lambda}(q)}{\sqrt{2M_{\rm Si}\Omega_\lambda(q)N}}(b_\lambda(q) + b_\lambda^\dagger(-q))e^{iqL}, \tag{28}$$

where L numerates atomic layers along the wire, a runs over the atoms within one layer, $b_\lambda(q)(b_\lambda^\dagger(q))$ is the annihilation (creation) operator for the λth phonon mode with wave number q, $\Omega_\lambda(q)$ is the phonon frequency, and $f_{a\lambda}(q)$ are the normalized phonon amplitudes $\sum_a f_{a\lambda}(q)f_{a\lambda'}(q) = \delta_{\lambda\lambda'}$. In Eq. (28), we ignore the difference between atomic layers in order to reduce the computational burden of constructing the self-energies. Assuming some "average" amplitude distribution $f_{a\lambda}(q) \approx f_a$ and dispersionless phonon modes we obtain the layer-diagonal phonon Green's functions in the Keldysh's picture,

$$-i\langle T_K u_{aL}(t)u_{a'L'}(t')\rangle = \delta_{LL'}\frac{f_a f_{a'}}{2M_{\rm Si}}\sum_{\lambda=1}^{N_{\rm ph}}\frac{1}{\Omega_\lambda}\Phi_{\Omega_\lambda}(t-t'), \tag{29}$$

where $N_{\rm ph}$ is the number of effectively interacting phonon modes and Φ_{Ω_λ} are the usual equilibrium functions.[20] In particular, the lesser/bigger functions in the energy representation read

$$\Phi_\Omega^{\gtrless}(\omega) = -2\pi i[(N_\Omega + 1)\delta(\omega \mp \Omega) + N_\Omega\delta(\omega \pm \Omega)], \tag{30}$$

where N_Ω is the bosonic occupation factor.

The EM phonon self-energies can be derived from the interaction term Eq. (26) in the basis representation Eq. (21) or obtained directly from the TBM self-energies,

$$\sigma_{\rm ph}^{\gtrless} = \hat{\Phi}^T \Sigma_{\rm ph}^{\gtrless}\hat{\Phi}. \tag{31}$$

In the self-consistent Born approximation, the lesser/bigger self-energies read

$$\Sigma_{ij}^{\gtrless}(\varepsilon) = i\int\frac{d\omega}{2\pi}\sum_{kl}\tilde{T}_{ik}G_{kl}^{\gtrless}(\varepsilon-\omega)\tilde{T}_{lj} \times[D_{il}^{\gtrless}(\omega) + D_{kj}^{\gtrless}(\omega) - D_{ij}^{\gtrless}(\omega) - D_{kl}^{\gtrless}(\omega)], \tag{32}$$

where the phonon Green's function $D_{ij}^{\gtrless}$ are given by Eqs. (29) and (30). The retarded self-energy $\sigma_{\rm ph}^R$ can be obtained by the Hilbert transform.[38] Here we follow the common approach and approximate σ_c^R by its anti-Hermitian part,[39]

$$\sigma_{\rm ph}^R = \tfrac{1}{2}(\sigma_{\rm ph}^> - \sigma_{\rm ph}^<). \tag{33}$$

Equations (31) and (22) define the EM self-energies in terms of the EM Green's functions and give a closed set of the NEGF equations. As follows from the tight-binding nearest-neighbor connection and the localized phonon Green's functions, the EM self-energies have the same tri-diagonal block structure as the one-particle device Hamiltonian. Thus, the EM NEGF equations can be solved easily. The phonon energies and the number of modes in Eq. (29) are free parameters of our model.

We have performed the self-consistent NEGF simulations using the one- and two-frequency models with the Green's functions,

$$D_{ij}^{\gtrless}(\omega) = \frac{\delta_{LL'}N_{\rm ph}f_a f_{a'}}{2M_{\rm Si}}\begin{cases}\dfrac{1}{\Omega}\Phi_\Omega^{\gtrless}(\omega),\\ \dfrac{1}{2\Omega_1}\Phi_{\Omega_1}^{\gtrless}(\omega) + \dfrac{1}{2\Omega_2}\Phi_{\Omega_2}^{\gtrless}(\omega).\end{cases} \tag{34}$$

$N_{\rm ph}$ has been taken as the number of atoms in one atomic layer. We have calculated two one-frequency models with $\Omega_1 = 20$ meV and $\Omega_2 = 60$ meV, which are likely to be the main peaks in the realistic phonon spectrum of SiNW.[18] The same frequencies have been used in the two-frequency model. We mimic free-surface boundary conditions by setting

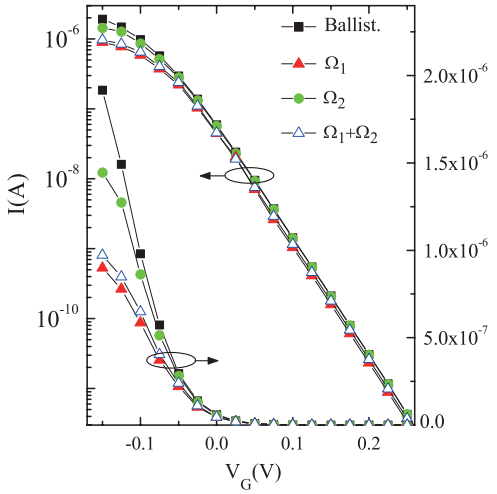

FIG. 11. (Color online) I-V characteristics of a p-SiNW FET. The black squares show ballistic current. Other marks refer to the one-frequency and two-frequency models of the electron-phonon scattering.

$f_a = f_0\rho_a$, where ρ_a is the radial distance of the ath atom from the central axis of the wire and f_0 is fixed by the normalization. Figure 11 shows the calculated drain current in the presence of electron-phonon scattering. The ballistic current is shown for comparison. At each electrostatic potential, five to ten self-consistent Born iterations of the Green's functions and phonon self-energies were enough to ensure convergence. The self-consistent coupling of the hole density and the device electrostatics is obtained though solving the Poisson equation. One can see significant reduction of the ON current, especially in the models with low-frequency mode ($I_{\rm ph}/I_{\rm ballist} \sim 0.5$). The calculations were repeated for the same models but with constant phonon amplitudes $f_a = 1/4\sqrt{2}$ and similar results were found except for somewhat smaller ON current ($I_{\rm ph}/I_{\rm ballist} \sim 0.4$). The stronger electron-phonon scattering in this case is due to larger phonon amplitudes in the middle of channel, where the major portion of current flows. The obtained ballisticity and the requisite number of iterations in the self-consistent Born approximation seem reasonable and justify the choice of physical parameters in our simple model. We have used the one-frequency model with the strongest effect (red solid triangles in Fig. 11) to test the EM convergence. To make a direct comparison, we have performed the self-consistent Born iterations using three EMs of the same TBM device Hamiltonian. Figure 12 shows the drain current calculated in the 17D and 36D EMs. The electrostatic potentials at different V_G were taken from the 17D EM ballistic simulations. In the nonballistic regime, the kinetic equation [Eq. (24)] involves the whole retarded Green's function. An undercomplete basis cannot generally reproduce solutions of the inhomogeneous Dyson equation, and one might expect that convergent EM simulations would require much larger EMs compared to the ballistic regime. This is not the case in Fig. 12, which shows a remarkable agreement between the two lowest models. In particular, at low V_G we obtain the same $\sim$1% agreement as in the ballistic regime. Note that the ON current $I_{\rm ph}$ is larger as compared to the full self-consistent calculations (Fig. 11). This difference is due

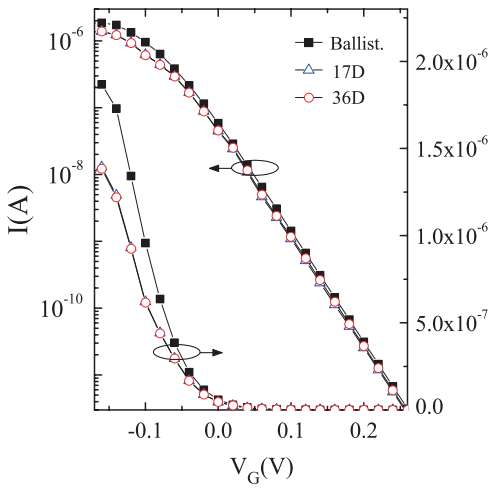

FIG. 12. (Color online) Nonballistic current in two EMs for the same TBM Hamiltonian with single-energy phonons (Ω_1 model in Fig. 11). The 17D and 36D EMs start to diverge in the subthreshold area $V_G > 0.05$ V. The ballistic current agrees at all V_G.

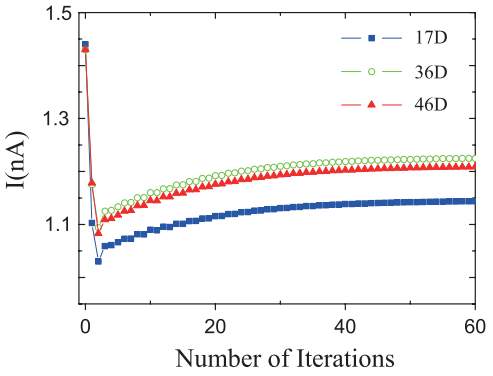

FIG. 13. (Color online) Self-consistent Born iterations for the drain current in Fig. 12 at $V_G = 0.1$ V. Comparison with the larger 46D EM confirms convergence of the EM calculations with respect to the basis size.

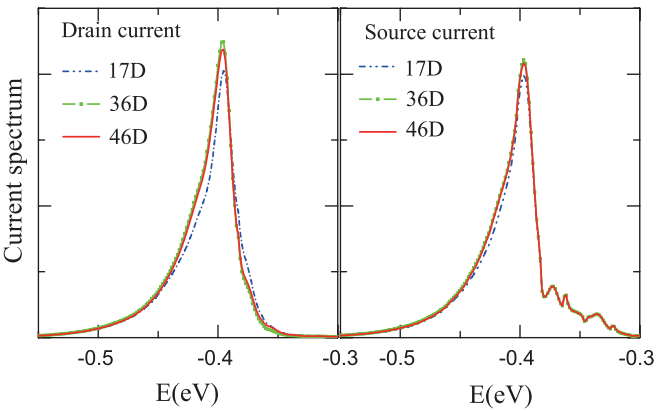

FIG. 14. (Color online) Nonballistic current spectra at source and drain contacts in three equivalent models.

to a shift of the band edge in the full calculations caused by the increased backscattering in agreement with earlier studies.[18] In the subthreshold region, the 17D and 36D EMs start to deviate but the difference never exceeds ∼10% and even in the worse case the 17D EM seems to give qualitatively correct results. The calculations were repeated with the larger 46D EM in order to verify convergence of the OFF current. As an illustration, we present in Fig. 13 the Born iterations of nonballistic current in three EMs at $V_G = 0.1$ V. The figure clearly demonstrates convergence with respect to the number of iteration steps and the model size. The 0th iteration corresponds to the ballistic regime where all three models are almost identical. In the presence of electron-phonon interaction, the 17D EM underestimates the current but the larger models agree very well. We have confirmed that the current density and the mobile charge in these two models coincide within a few percent. Figure 14 shows an example of the current spectrum at two contacts after the last iteration. The two spectra are different since, unlike the ballistic regime, the current in the presence of inelastic scattering is not conserved at each energy. The 17D EM underestimate the nonballistic current at lower energies due to not-wide-enough spectrum of scattering states in this model. The current spectrum in the 17D EM is only qualitatively correct, but the 36D and 46D EMs reproduce each other very well. Interestingly, even the smallest EM gives a correct phonon emission subband structure at the source contact. In the drain region, these oscillations are smoothed out giving rise to a shift of the right wing toward higher energies. This reflects a general tendency of the current spectrum to follow the contour of the electrostatic potential in the presence of inelastic processes. The spectral changes along the wire are more conspicuous in ON states.[18]

V. CONCLUDING REMARKS

We have reported a basis representation of the tight-binding Hamiltonian in quantum wires. Starting from the individual atomic orbitals, we have constructed a low-dimensional basis of relevant functions which give correct physics of the NW device. The numerical tests have confirmed that accurate atomistic transport simulations can be performed using ∼1% of the total number of orbitals in the nanostructure. This greatly reduces the computational burden and allows inelastic effects to be incorporated.

The present approach rests on the assumption that quantum transport can be described in terms of transitions between scattering states in an ideal wire. We can thus obtain the EM basis by analyzing the Bloch Hamiltonian for a single unit-structure in the ideal wire. Treating NWs with variable diameter requires modification of this approach. Surface-roughness-induced variability in NWs is another interesting problem which can be reduced to constructing a scattering self-energy in the EM Hamiltonian. Statistical properties of this term and limitations of the EM approach in such a case have not been studied yet. Finally, it is worth noting that the variational method of Sec. III is quite general as it gives a regular way to build a small quantum model which reproduces physical properties of an arbitrary family of Hamiltonians within an arbitrary energy window. This may find other applications in problems of quantum kinetics and electronic structure calculations.

*gena@si.eei.eng.osaka-u.ac.jp

[1] N. Lindert, L. Chang, Y.-K. Choi, E. H. Anderson, W.-C. Lee, T.-J. King, J. Bokor, and C. Hu, IEEE Electron Device Lett. **22**, 487 (2001).
[2] P. L. McEuen, M. S. Fuhrer, and H. K. Park, IEEE Trans. Nanotechnol. **1**, 78 (2002).
[3] Y. Cui, Z. Zhong, D. Wang, J. Wang, and C. M. Lieber, Nano Lett. **3**, 149 (2003).
[4] Y. Wu, Y. Cui, L. Huynh, C. Barrelet, D. Bell, and C. Lieber, Nano Lett. **4**, 433 (2004).
[5] D. Ma, C. S. Lee, F. K. Au, S. T. Tong, and S. T. Lee, Science **299**, 1874 (2003).
[6] J. D. Holmes, K. Johnston, R. C. Doty, and B. A. Korgel, Science **287**, 1471 (2000).
[7] K. H. Cho, K. H. Yeo, Y. Y. Yeoh, S. D. Suk, M. Li, J. M. Lee, M. S. Kim, D. W. Kim, D. Park, B. H. Hong, Y. C. Jung, and S. W. Hwang, Appl. Phys. Lett. **92**, 052102 (2008).
[8] M. Konayashi and T. Hiramoto, J. Appl. Phys. **103**, 053709 (2008).
[9] N. Singh, A. Agarwal, L. K. Bera, T. Y. Liow, R. Yang, S. C. Rustagi, C. H. Tung, R. Kumar, G. Q. Lo, N. Balasubramanian, and D. L. Kwong, IEEE Electron Device Lett. **27**, 383 (2006).
[10] J. Xiang, W. Lu, Y. Hu, Y. Wu, H. Yan, and C. M. Lieber, Nature (London) **441**, 489 (2006).
[11] K. A. Dick, K. Deppert, T. Martensson, B. Mandl, L. Samuelson, and W. Seifert, Nano Lett. **5**, 761 (2005).
[12] M. S. Gudiksen, L. J. Lauhon, J. Wang, D. C. Smith, and C. M. Lieber, Nature (London) **415**, 617 (2002).
[13] Y. Wu, R. Fan, and P. Yang, Nano Lett. **2**, 83 (2002).
[14] N. Neophytou, S. G. Kim, G. Klimeck, and H. Kosina, J. Appl. Phys. **107**, 113701 (2010).
[15] M. Lundstrom and J. Guo, *Nanoscale Transistors: Device Physics, Modeling, and Simulation* (Springer, New York, 2006).
[16] J. Kröger, Rep. Prog. Phys. **69**, 899 (2006).
[17] S. D. Suk, M. Li, Y. Y. Yeoh, K. H. Yeo, K. H. Cho, I. K. Ku, H. Cho, W. Jang, D.-W. Kim, D. Park, and W.-S. Lee, IEDM Tech. Dig. 891 (2007).
[18] M. Luisier and G. Klimeck, Phys. Rev. B **80**, 155430 (2009).
[19] A. Pecchia and A. Di Carlo, Rep. Prog. Phys. **67**, 1497 (2004).
[20] H. Haug and A. P. Jauho, *Quantum Kinetics in Transport and Optics of Semiconductors* (Springer-Verlag, Berlin, 1998).
[21] S. Datta, *Electronic Transport in Mesoscopic Systems* (Cambridge University Press, Cambridge, 1995).
[22] S. Rotter, J. Z. Tang, L. Wirtz, J. Trost, and J. Burgdörfer, Phys. Rev. B **62**, 1950 (2000).
[23] A. Svizhenko, M. P. Anantram, T. R. Govindan, B. Biegel, and R. Venugopal, J. Appl. Phys. **91**, 2343 (2002).
[24] G. V. Mil'nikov, N. Mori, Y. Kamakura, and T. Ezaki, Appl. Phys. Express **1**, 063001 (2008).
[25] G. Mil'nikov, N. Mori, Y. Kamakura, and T. Ezaki, J. Appl. Phys. **104**, 044506 (2008).

[26]G. V. Mil'nikov, N. Mori, and Y. Kamakura, Phys. Rev. B **79**, 235337 (2009).
[27]A. Svizhenko and M. P. Anantram, Phys. Rev. B **72**, 085430 (2005).
[28]M. Pourfath, H. Kosina, and S. Selberherr, J. Comput. Electron. **6**, 321 (2007).
[29]S. Jin, Y. Park, and H. Min, J. Appl. Phys. **99**, 123719 (2006).
[30]C. Rivas and R. Lake, Phys. Status Solidi B **239**, 94 (2003).
[31]N. Marzari and D. Vanderbilt, Phys. Rev. B **56**, 12847 (1997).
[32]I. Souza, N. Marzari, and D. Vanderbilt, Phys. Rev. B **65**, 035109 (2002).
[33]K. S. Thygesen, L. B. Hansen, and K. W. Jacobsen, Phys. Rev. B **72**, 125119 (2005).
[34]I. Souza, R. M. Martin, N. Marzari, X. Zhao, and D. Vanderbilt, Phys. Rev. B **62**, 15505 (2000).
[35]A. Calzolari, N. Marzari, I. Souza, and M. B. Nardelli, Phys. Rev. B **69**, 035108 (2004).
[36]W. Zhang, C. Delerue, Y. M. Niquet, G. Allan, and E. Wang, Phys. Rev. B **82**, 115319 (2010).
[37]A. Valentin, J. See, S. Galdin-Retailleau, and P. Dollfus, J. Phys. Condens. Matter **20**, 145213 (2008).
[38]T. Frederiksen, M. Paulsson, M. Brandbyge, and A.-P. Jauho, Phys. Rev. B **75**, 205413 (2007).
[39]A. Svizhenko and M. P. Anantram, IEEE Trans. Electron Dev. **50**, 1459 (2007).